Applicable Analysis and Discrete Mathematics
available online at http://pefmath.etf.rs

Appl. Anal. Discrete Math. **19** (2025), 668–693.
https://doi.org/10.2298/AADM250214038S

BI-INERTIAL PROJECTIVE VISCOSITY FORWARD-BACKWARD SPLITTING ALGORITHM FOR PREDICTING SOUND ABSORPTION COEFFICIENT OF MATERIALS

*Raweerote Suparatulatorn, Nipa Jun-on, Siwat Lawanwadeekul, Watcharaporn Yajai, Watcharaporn Cholamjiak**

This study investigates the variational inclusion problem (VIP) and proposes improved inertial–relaxation algorithms that offer faster and more stable convergence. We apply these methods to predict the sound absorption coefficient (SAC) from non-acoustic material properties. Comparative experiments show that the proposed approach achieves the highest accuracy (86.67–91.43%) with superior computational efficiency. The results show that advanced optimization offers a cost-effective alternative to SAC testing.

1. INTRODUCTION

The ability to predict the sound absorption behavior of materials plays a crucial role in the design and development of materials for noise control across various industries, including construction, high-rise buildings, automotive engineering, and the audio industry. The acoustic properties of materials directly influence the efficiency of soundproofing systems and noise reduction strategies, which are essential for optimizing acoustic environments [**13, 14**].

*Corresponding author. Watcharaporn Cholamjiak
2020 Mathematics Subject Classification. 65K05, 90C30, 90B30.
Keywords and Phrases. Variational inclusion problem, Tseng's method, Non-acoustic property, Sound absorbtion coefficiency, Process innovation.

Traditionally, the measurement of a material's sound absorption properties follows internationally recognized standards such as ISO 354 [**31**], which employs the Reverberation Room Method, and ISO 10534-2:1998 [**32**], which utilizes the Impedance Tube Method. These methods provide empirical measurements of the sound absorption coefficient (SAC; α), a critical parameter indicating how effectively a material absorbs sound energy. While these approaches offer high accuracy, they require specialized equipment and controlled environments, making them time-consuming and costly.

Several researchers have developed mathematical models to predict the sound absorption coefficient based on material properties. In 1992, J. F. Allard and Y. Champoux [**1**] introduced a predictive model utilizing parameters such as porosity and flow resistivity to estimate the acoustic behavior of porous materials. Similarly, Trevor J. Cox and Peter D'Antonio [**7**] refined these models by incorporating additional parameters, including i) *material thickness*, which influences low-frequency absorption; ii) *flow resistivity*, which determines how air moves through the material, and iii) *air gap*, which affects sound reflection and absorption.

Despite the effectiveness of these approaches, they present several limitations. First, some parameters, such as flow resistivity, are difficult to measure and require complex experimental setups. Second, traditional models rely on idealized assumptions regarding material homogeneity, which may not hold true due to variations in material composition and manufacturing processes [**1, 7**]. As a result, conventional prediction methods may fail to accurately represent real-world material behavior.

Thus, to address the limitations of traditional methods, recent research has explored the potential of using non-acoustic parameters, or physical properties of materials, which are easier to measure and more cost-effective to obtain. These parameters include density, water absorption, porosity, and pore size distribution, all of which can be evaluated through standard material testing procedures. If these physical properties can be correlated with sound absorption characteristics, they could significantly reduce the complexity and cost of direct acoustic testing.

However, predicting sound absorption from non-acoustic parameters presents a significant challenge. The relationship between physical properties and acoustic performance is inherently multivariate and nonlinear, meaning that simple linear regression models may not be sufficient. Furthermore, manufacturing processes, additive materials, and microstructural variations contribute to the complexity of this relationship, making traditional estimation methods inadequate.

Given these challenges, the development of advanced mathematical algorithms is necessary to handle the complexity of non-acoustic data while ensuring accurate predictions.

Throughout this article, let $\mathcal{H}$ denote a real Hilbert space equipped with the inner product $\langle \cdot, \cdot \rangle$ and the associated norm $\| \cdot \|$. We denote by $\mathbb{R}$ and $\mathbb{N}$ the sets of real numbers and nonnegative integers, respectively.

The variational inclusion problem (shortly, VIP) is typically formulated as

follows:

$$\text{Find } \ v \in \mathcal{H} \ \text{ such that } \ 0 \in (X+Y)v, \tag{1}$$

where $X : \mathcal{H} \to \mathcal{H}$ is a single valued mapping and $Y : \mathcal{H} \to 2^{\mathcal{H}}$ is a multivalued mapping. The set of all solutions to the VIP is denoted by $(X+Y)^{-1}(0)$.

The study of solving the VIP has garnered significant attention among researchers in optimization and functional analysis. Numerous researchers have focused on developing efficient algorithms for addressing this problem. Two methods that have gained considerable popularity are the forward-backward splitting method [**15, 21**] and the Tseng splitting method [**28**]. Various researchers have modified and adapted the forward-backward splitting method to solve the VIP (see [**5, 8, 16, 23, 19**]). The Tseng splitting method is another approach that has been refined and applied to solve the VIP (see [**4, 20, 24**]). Both methodologies are extensively referenced in the academic literature on solving the VIP, owing to their efficiency and flexibility in application to various problem formulations. Researchers have further developed these methods, enhancing convergence rates, computational error tolerance, and the capacity to accommodate additional problem constraints. Recently, Kesornprom and Cholamjiak [**12**] introduced the following IMRFB for solving the VIP in the case where $X = \nabla f$ and $Y = \partial g$, where $f : \mathcal{H} \to \mathbb{R}$ is a convex and differentiable function with a Lipschitz continuous gradient and $g : \mathcal{H} \to (-\infty, +\infty]$ is a proper, lower semicontinuous, and convex function. Moreover, this algorithm has been applied to solve X-ray image inpainting.

More recently, Peeyada et al. [**22**] introduced the following TIPMFB, modified from the forward-backward algorithm and the two-step inertial proximal point algorithm [**11**], for solving the VIP in the case where X is η-inverse strongly monotone and Y is a maximal monotone mapping. This algorithm has been proven to converge weakly under some standard and mild conditions and has been used for stroke prediction by an extreme learning machine.

The viscosity approximation method [**18**] is an important technique in fixed-point theory and optimization, particularly when strong convergence to a solution is desired. In 2018, Gibali and Thong [**9**] introduced a modification of the Tseng splitting method based on the viscosity approximation method for solving the VIP and established the strong convergence of the proposed algorithm under standard assumptions. Moreover, this algorithm has been applied to solve the problem of recovering a sparse noisy signal.

2. PRELIMINARIES

In this section, we introduce fundamental definitions and concepts that will be used throughout the paper, including metric projection, monotone operators, and self-mappings in Hilbert spaces $\mathcal{H}$.

Algorithm 1 : Inertial modified relaxed forward-backward-forward method (IMRFB)

Initialization: Let $a_0 = a_1 \in \mathcal{H}$, $\lambda_1 > 0$, $\theta_1 \geq 0$, and $\mu, \rho_n \in (0,1)$.
Iterative Steps: Let S be a nonempty, closed, and convex subset of $\mathcal{H}$. Given $n \geq 1$, calculate a_{n+1} as follows:
Step 1. Compute the inertial step:

$$w_n = a_n + \theta_n(a_n - a_{n-1}).$$

Step 2. Compute the forward-backward-forward step:

$$\begin{aligned} y_n &= \text{prox}_{\lambda_n g}(w_n - \lambda_n \nabla f(w_n)), \\ z_n &= (1-\rho_n)w_n + \rho_n(y_n - \lambda_n(\nabla f(y_n) - \nabla f(w_n))). \end{aligned}$$

Step 3. Compute the projection step:

$$a_{n+1} = P_S(z_n).$$

Step 4. Compute the stepsize step:

$$\lambda_{n+1} = \begin{cases} \min\left\{\lambda_n, \dfrac{\mu\|y_n - w_n\|}{\|\nabla f(y_n) - \nabla f(w_n)\|}\right\} & \text{if } \nabla f(y_n) - \nabla f(w_n) \neq 0; \\ \lambda_n & \text{otherwise.} \end{cases}$$

Set $n = n+1$ and return to **Step 1.**

Algorithm 2 : Two inertial projective Mann forward-backward algorithm (TIPMFB)

Initialization: Let S be a nonempty, closed, and convex subset of $\mathcal{H}$. Let $a_{-1}, a_0, a_1 \in \mathcal{H}$, $\alpha_n \in (a,b) \subset (0,1]$, $r_n \in (c,d) \subset (0, 2\eta)$ $\theta_n, \delta_n \in (-\infty, \infty)$ satisfy the following conditions:

$$\sum_{n=1}^{\infty} |\theta_n| \|a_n - a_{n-1}\| < \infty \text{ and } \sum_{n=1}^{\infty} |\delta_n| \|a_{n-1} - a_{n-2}\| < \infty.$$

Iterative Steps:
Step 1. Compute

$$y_n = a_n + \theta_n(a_n - a_{n-1}) + \delta_n(a_{n-1} - a_{n-2}).$$

Step 2. Compute

$$a_{n+1} = P_S((1-\alpha_n)a_n + \alpha_n(I + r_n Y)^{-1}(I - r_n X)y_n).$$

Set $n = n+1$ and return to **Step 1.**

Definition 2.1. [**25**] Let S be a nonempty, closed, and convex subset of $\mathcal{H}$. For every $u \in \mathcal{H}$, define the metric projection P_S from $\mathcal{H}$ onto S by

$$P_S(u) := \arg\min_{v \in S} \|u - v\|.$$

Definition 2.2. [**25**] A multivalued mapping $Y : \mathcal{H} \to 2^{\mathcal{H}}$ is defined as follows:

(*i*) Y is called monotone if, for every pair $(p, q), (v, u) \in graph(Y)$, the following inequality holds:

$$\langle q - u, p - v \rangle \geq 0.$$

(*ii*) Y is called maximally monotone if it is monotone and there is no other monotone operator that properly contains it. In other words, Y is maximally monotone if, for every $(p, q) \in \mathcal{H} \times \mathcal{H}$, the condition

$$\langle q - u, p - v \rangle \geq 0 \quad \text{for all} \quad (v, u) \in graph(Y)$$

implies that $(p, q) \in graph(Y)$.

Definition 2.3. [**6**] A self-mapping $X : \mathcal{H} \to \mathcal{H}$ is defined as follows:

(*i*) X is called firmly nonexpansive if, for all $p, q \in \mathcal{H}$, it satisfies:

$$\|Xp - Xq\|^2 \leq \|p - q\|^2 - \|(I - X)p - (I - X)q\|^2.$$

(*ii*) X is called β-cocoercive if there exists a constant $\beta > 0$ such that, for all $p, q \in \mathcal{H}$, the following inequality holds:

$$\langle Xp - Xq, p - q \rangle \geq \beta \|Xp - Xq\|^2.$$

(*iii*) X is called L-Lipschitz continuous if there exists a constant $L > 0$ such that, for all $p, q \in \mathcal{H}$, the following inequality holds:

$$\|Xp - Xq\| \leq L\|p - q\|.$$

(*iv*) X is called L-contraction if it is L-Lipschitz continuous with $0 < L < 1$.

(*v*) X is called nonexpansive if it is 1-Lipschitz continuous.

Lemma 2.4. [**29**] *Let $\{s_n\}$ be a sequence of non-negative real numbers satisfying*

$$s_{n+1} \leq (1 - \alpha_n)s_n + \alpha_n\beta_n + \gamma_n, \quad n \in \mathbb{N},$$

where $\{\alpha_n\}$, $\{\beta_n\}$, and $\{\gamma_n\}$ satisfy the conditions:

(*i*) $\{\alpha_n\} \subset [0, 1]$, $\sum_{n=1}^{\infty} \alpha_n = \infty$, *or equivalently,* $\prod_{n=1}^{\infty} (1 - \alpha_n) = 0$;

(*ii*) $\limsup_{n\to\infty} \beta_n \leq 0$;

(*iii*) $\gamma_n \geq 0$, $\sum_{n=1}^{\infty} \gamma_n < \infty$.

Then $\lim_{n\to\infty} s_n = 0$.

Lemma 2.5. [**17**] *Let* (τ_n) *be a sequence of real numbers that does not decrease at infinity, in the sense that there exists a subsequence* $(\tau_{n_j})_{j\geq 0}$ *of* (τ_n) *such that*

$$\tau_{n_j} < \tau_{n_j+1} \quad \text{for all} \quad j \geq 0.$$

Also consider the sequence of integers $(\tau^*(n))_{n\geq n_0}$ *defined by*

$$\tau^*(n) = \max\{k \leq n \mid \tau_k < \tau_{k+1}\}.$$

Then $(\tau^*(n))_{n\geq n_0}$ *is a nondecreasing sequence verifying*

$$\lim_{n\to\infty} \tau^*(n) = \infty,$$

and, for all $n \geq n_0$, *the following two estimates hold:*

$$\tau_{\tau^*(n)} \leq \tau_{\tau^*(n)+1},$$

$$\tau_n \leq \tau_{\tau^*(n)+1}.$$

3. MAIN RESULTS

We now turn to the theoretical analysis of the algorithm introduced in this work. To establish its convergence properties, we begin by stating the following conditions, which form the basis for our subsequent proofs.

($\mathcal{C}1$) $Y : \mathcal{H} \to 2^{\mathcal{H}}$ is maximal monotone mapping.

($\mathcal{C}2$) S is nonempty, closed and convex subset of $\mathcal{H}$.

($\mathcal{C}3$) $X : \mathcal{H} \to \mathcal{H}$ is β-cocoercive mapping.

($\mathcal{C}4$) $\phi : \mathcal{H} \to \mathcal{H}$ is ϱ-Lipschitz continuous, where $\varrho \in [0, 1)$.

($\mathcal{C}5$) $\Psi := S \cap (X + Y)^{-1}(0)$ is nonempty.

The following algorithm will be employed for Theorem 3.6.

Next, we are ready to prove Theorem 3.6.

Algorithm 3

Initialization: Select arbitrary elements $a_{-1}, a_0, a_1 \in \mathcal{H}$. Let $\{\alpha_n\} \subset (0,1)$, $\{\mu_n\} \subset (0, 2\beta)$, $\{\theta_n\}, \{\delta_n\} \subset (-\infty, \infty)$ and set $n := 1$.
Iterative Steps: Construct $\{a_n\}$ by using the following steps:
Step 1. Define

$$d_n = a_n + \theta_n(a_n - a_{n-1}) + \delta_n(a_{n-1} - a_{n-2}).$$

Step 2. Compute

$$b_n = (I + \mu_n Y)^{-1}(I - \mu_n X)d_n.$$

Step 3. Evaluate

$$a_{n+1} = P_S[\alpha_n \phi(a_n) + (1 - \alpha_n)b_n].$$

If $b_n = d_n = P_S d_n$ then stop and $d_n \in \Psi$. Otherwise, replace n by $n + 1$ and then repeat **Step 1.**

Theorem 3.6. *Let the sequence $\{a_n\}$ be generated by Algorithm 3 satisfying the items $(\mathcal{C}1) - (\mathcal{C}5)$. Assume that the following conditions are satisfied:*

$(\mathcal{C}6)$ $0 < \liminf_{n\to\infty} \mu_n \leq \limsup_{n\to\infty} \mu_n < 2\beta$.

$(\mathcal{C}7)$ $\lim_{n\to\infty} \alpha_n = \lim_{n\to\infty} \frac{\theta_n}{\alpha_n}\|a_n - a_{n-1}\| = \lim_{n\to\infty} \frac{\delta_n}{\alpha_n}\|a_{n-1} - a_{n-2}\| = 0$.

$(\mathcal{C}8)$ $\sum_{n=1}^{\infty} \alpha_n = \infty$.

Then, $\{a_n\}$ converges strongly to $\tilde{a}$, where $\tilde{a} = P_\Psi(\phi(\tilde{a}))$.

Proof. Let $a^* \in \Psi$. According to [**2**], we have $(I + \mu_n Y)^{-1}$ is a single-valued firmly nonexpansive mapping and $a^* = (I+\mu_n Y)^{-1}(I-\mu_n X)a^*$. Since X is a β-cocoercive mapping, we obtain

$$\begin{aligned}
\|b_n - a^*\|^2 &= \|(I + \mu_n Y)^{-1}(I - \mu_n X)d_n - (I + \mu_n Y)^{-1}(I - \mu_n X)a^*\|^2 \\
&\leq \|d_n - a^* - \mu_n(Xd_n - Xa^*)\|^2 - \|d_n - b_n - \mu_n(Xd_n - Xa^*)\|^2 \\
&= \|d_n - a^*\|^2 - 2\mu_n\langle d_n - a^*, Xd_n - Xa^*\rangle + \mu_n\|Xd_n - Xa^*\|^2 \\
&\quad - \|d_n - b_n - \mu_n(Xd_n - Xa^*)\|^2 \\
&\leq \|d_n - a^*\|^2 - \mu_n(2\beta - \mu_n)\|Xd_n - Xa^*\|^2 - \|d_n - b_n - \mu_n(Xd_n - Xa^*)\|^2. \qquad (2)
\end{aligned}$$

Based on $(\mathcal{C}7)$, we have $\lim_{n\to\infty} \Xi_n = \lim_{n\to\infty} \alpha_n \Xi_n = 0$, where $\Xi_n := \alpha_n^{-1}(|\theta_n|\|a_n - a_{n-1}\| + |\delta_n|\|a_{n-1} - a_{n-2}\|)$. This immediately implies that both $\{\Xi_n\}$ and $\{\alpha_n \Xi_n\}$ are bounded.

Thus, from (2) and $\{\mu_n\} \subset (0, 2\beta)$, it follows that there exists a $B_1 > 0$ such that

$$\|b_n - a^*\| \leq \|d_n - a^*\| \leq \|a_n - a^*\| + \alpha_n \Xi_n \leq \|a_n - a^*\| + \alpha_n B_1. \tag{3}$$

This inequality, combined with the ϱ-contractivity of ϕ and the nonexpansiveness of P_S, leads to the following calculation:

$$\begin{aligned}
\|a_{n+1} - a^*\| &= \|P_S(y_n) - P_S(a^*)\| \\
&\leq \|y_n - a^*\| \\
&\leq \alpha_n \|\phi(a_n) - \phi(a^*)\| + \alpha_n \|\phi(a^*) - a^*\| + (1 - \alpha_n)\|b_n - a^*\| \\
&\leq \alpha_n \varrho \|a_n - a^*\| + \alpha_n \|\phi(a^*) - a^*\| + (1 - \alpha_n)(\|a_n - a^*\| + \alpha_n B_1) \\
&\leq (1 - \tilde{\alpha}_n)\|a_n - a^*\| + \alpha_n(\|\phi(a^*) - a^*\| + B_1) \\
&= (1 - \tilde{\alpha}_n)\|a_n - a^*\| + \tilde{\alpha}_n B_2 \\
&\leq \max\{\|a_n - a^*\|, B_2\},
\end{aligned}$$

where $y_n := \alpha_n \phi(a_n) + (1 - \alpha_n) b_n$, $\tilde{\alpha}_n := \alpha_n(1 - \varrho)$, and $B_2 := \dfrac{\|\phi(a^*) - a^*\| + B_1}{1 - \varrho}$. Thus, $\|a_{n+1} - a^*\| \leq \max\{\|a_1 - a^*\|, B_2\}$. Therefore, $\{\|a_n - a^*\|\}$ is bounded. This result, together with (3) and $\{\alpha_n \Xi_n\}$ is bounded, implies that

$$\begin{aligned}
\|b_n - a^*\|^2 \leq \|d_n - a^*\|^2 &\leq [\|a_n - a^*\| + \alpha_n \Xi_n]^2 \\
&= \|a_n - a^*\|^2 + \alpha_n \Xi_n (2\|a_n - a^*\| + \alpha_n \Xi_n) \\
&\leq \|a_n - a^*\|^2 + \alpha_n \Xi_n B_3
\end{aligned} \tag{4}$$

for some $B_3 > 0$. Since Ψ is nonempty, closed, and convex, and by applying the Banach contraction principle, we obtain that there exists a unique $\tilde{a} \in \Psi$ such that $\tilde{a} = P_\Psi(\phi(\tilde{a}))$. According to the characterization of P_Ψ, the following inequality holds for any $b \in \Psi$:

$$\langle \phi(\tilde{a}) - \tilde{a}, b - \tilde{a} \rangle \leq 0. \tag{5}$$

By employing (4), we derive

$$\begin{aligned}
\|a_{n+1} - \tilde{a}\|^2 &\leq \|y_n - \tilde{a}\|^2 \\
&\leq \|\alpha_n(\phi(a_n) - \phi(\tilde{a})) + (1 - \alpha_n)(b_n - \tilde{a})\|^2 + 2\alpha_n \langle \phi(\tilde{a}) - \tilde{a}, y_n - \tilde{a} \rangle \\
&\leq \alpha_n \|\phi(a_n) - \phi(\tilde{a})\|^2 + (1 - \alpha_n)\|b_n - \tilde{a}\|^2 + 2\alpha_n \langle \phi(\tilde{a}) - \tilde{a}, y_n - \tilde{a} \rangle \\
&\leq \alpha_n \varrho^2 \|a_n - \tilde{a}\|^2 + (1 - \alpha_n)[\|a_n - \tilde{a}\|^2 + \alpha_n \Xi_n B_3] + 2\alpha_n \langle \phi(\tilde{a}) - \tilde{a}, y_n - \tilde{a} \rangle \\
&\leq \alpha_n \varrho \|a_n - \tilde{a}\|^2 + (1 - \alpha_n)\|a_n - \tilde{a}\|^2 + \alpha_n \Xi_n B_3 + 2\alpha_n \langle \phi(\tilde{a}) - \tilde{a}, y_n - \tilde{a} \rangle \\
&= (1 - \tilde{\alpha}_n)\|a_n - \tilde{a}\|^2 + \tilde{\alpha}_n (1 - \varrho)^{-1} [\Xi_n B_3 + 2\langle \phi(\tilde{a}) - \tilde{a}, y_n - \tilde{a} \rangle].
\end{aligned} \tag{6}$$

Combining (2) with (4), we deduce

$$\begin{aligned}
\|a_{n+1} - \tilde{a}\|^2 &\leq \alpha_n \|\phi(a_n) - \tilde{a}\|^2 + (1 - \alpha_n)\|b_n - \tilde{a}\|^2 \\
&\leq \alpha_n \|\phi(a_n) - \tilde{a}\|^2 + \|b_n - \tilde{a}\|^2 \\
&\leq \|d_n - \tilde{a}\|^2 + \alpha_n \|\phi(a_n) - \tilde{a}\|^2 \\
&\quad - \mu_n(2\beta - \mu_n)\|Xd_n - X\tilde{a}\|^2 - \|d_n - b_n - \mu_n(Xd_n - X\tilde{a})\|^2 \\
&\leq \|a_n - \tilde{a}\|^2 + \alpha_n(\Xi_n B_3 + \|\phi(a_n) - \tilde{a}\|^2) \\
&\quad - \mu_n(2\beta - \mu_n)\|Xd_n - X\tilde{a}\|^2 - \|d_n - b_n - \mu_n(Xd_n - X\tilde{a})\|^2
\end{aligned} \tag{7}$$

Following the recent inequality, where $\{\Xi_n\}$ and $\{\|\phi(a_n)-\tilde{a}\|^2\}$ are bounded, we find that there exists a $B_4 > 0$ such that

$$\begin{aligned}\mu_n(2\beta-\mu_n)\|Xd_n - X\tilde{a}\|^2 + \|d_n - b_n - \mu_n(Xd_n - X\tilde{a})\|^2 \\ \leq \|a_n - \tilde{a}\|^2 - \|a_{n+1} - \tilde{a}\|^2 + \alpha_n B_4.\end{aligned} \tag{8}$$

Case 1. Consider an $N \in \mathbb{N}$ such that $\|a_{n+1} - \tilde{a}\|^2 \leq \|a_n - \tilde{a}\|^2$ holds for every $n \geq N$. This demonstrates that $\lim_{n\to\infty} \|a_n - \tilde{a}\|^2$ exists. Referring to $(\mathcal{C}6)$ and $(\mathcal{C}7)$ in combination with (8), we determine that

$$\lim_{n\to\infty} \|Xd_n - X\tilde{a}\| = \lim_{n\to\infty} \|d_n - b_n - \mu_n(Xd_n - X\tilde{a})\| = 0.$$

This leads directly to the conclusion that

$$\lim_{n\to\infty} \|d_n - b_n\| = 0. \tag{9}$$

With the recent result and $\lim_{n\to\infty} \alpha_n \Xi_n = 0$, it can be deduced that

$$\begin{aligned}\|b_n - a_n\| &\leq \|b_n - d_n\| + \|d_n - a_n\| \\ &\leq \|b_n - d_n\| + \alpha_n \Xi_n \to 0 \text{ as } n \to \infty.\end{aligned} \tag{10}$$

As $\{\|\phi(a_n) - a_n\|\}$ is bounded, we have

$$\begin{aligned}\|y_n - a_n\| &\leq \alpha_n\|\phi(a_n) - a_n\| + (1-\alpha_n)\|b_n - a_n\| \\ &\leq \alpha_n B_5 + \|b_n - a_n\|\end{aligned}$$

for some $B_5 > 0$. Taking the limit and utilizing (10) in conjunction with $(\mathcal{C}7)$, we conclude that

$$\lim_{n\to\infty} \|y_n - a_n\| = 0. \tag{11}$$

Since $\{a_n\}$ is bounded, there is a point $y^* \in \mathcal{H}$ such that $a_{n_k} \rightharpoonup y^*$ as $k \to \infty$ for some subsequence $\{a_{n_k}\}$ of $\{a_n\}$. This implies by (10) that $b_{n_k} \rightharpoonup y^*$ as $k \to \infty$. From $a_{n+1} \in S$ and S is closed, we get that $y^* \in S$. From [**30**], if X is a β-cocoercive mapping, then X is $\frac{1}{\beta}$-Lipschitz continuous and monotone. This result, combined with Y being a maximal monotone mapping as noted in [**3**], implies that $X + Y$ is a maximal monotone mapping. Next, we show that $y^* \in (X+Y)^{-1}(0)$. Let $(v,u) \in graph\,(X+Y)$, that is, $u - Xv \in Yv$. It implies by the definition of b_n that $\frac{1}{\mu_{n_k}}(d_{n_k} - b_{n_k} - \mu_{n_k} Xd_{n_k}) \in Yb_{n_k}$. By the monotonicity of Y, we have

$$\left\langle v - b_{n_k}, u - Xv - \frac{1}{\mu_{n_k}}(d_{n_k} - b_{n_k} - \mu_{n_k} Xd_{n_k}) \right\rangle \geq 0.$$

Thus, by the monotonicity of X, we get

$$\begin{aligned}\langle v - b_{n_k}, u\rangle &\geq \left\langle v - b_{n_k}, Xv + \frac{1}{\mu_{n_k}}(d_{n_k} - b_{n_k} - \mu_{n_k} Xd_{n_k}) \right\rangle \\ &= \langle v - b_{n_k}, Xv - Xb_{n_k}\rangle + \langle v - b_{n_k}, Xb_{n_k} - Xd_{n_k}\rangle + \frac{1}{\mu_{n_k}}\langle v - b_{n_k}, d_{n_k} - b_{n_k}\rangle \\ &\geq \langle v - b_{n_k}, Xb_{n_k} - Xd_{n_k}\rangle + \frac{1}{\mu_{n_k}}\langle v - b_{n_k}, d_{n_k} - b_{n_k}\rangle.\end{aligned}$$

Using (9) and the fact that X is Lipschitz continuous, we conclude that $\lim_{k\to\infty} \|Xb_{n_k} - Xd_{n_k}\| = 0$. Furthermore, since $\liminf_{k\to\infty} \mu_{n_k} > 0$, we have

$$\langle v - y^*, u\rangle = \lim_{k\to\infty} \langle v - b_{n_k}, u\rangle \geq 0,$$

which, combined with the maximal monotonicity of $X+Y$, implies that $y^* \in (X+Y)^{-1}(0)$. Hence, $y^* \in \Psi$. By (5), we have

$$\limsup_{n\to\infty} \langle \phi(\tilde{a}) - \tilde{a}, a_n - \tilde{a}\rangle = \lim_{k\to\infty} \langle \phi(\tilde{a}) - \tilde{a}, a_{n_k} - \tilde{a}\rangle = \langle \phi(\tilde{a}) - \tilde{a}, y^* - \tilde{a}\rangle \leq 0.$$

Using (11), we obtain

$$\limsup_{n\to\infty} \langle \phi(\tilde{a}) - \tilde{a}, y_n - \tilde{a}\rangle \leq \limsup_{n\to\infty} \langle \phi(\tilde{a}) - \tilde{a}, y_n - a_n\rangle + \limsup_{n\to\infty} \langle \phi(\tilde{a}) - \tilde{a}, a_n - \tilde{a}\rangle \leq 0.$$

Applying this to (6) with Lemma 2.4, we can conclude that $\lim_{n\to\infty} \|a_n - \tilde{a}\| = 0$.

Case 2. Consider a subsequence $\{\|a_{n_q} - \tilde{a}\|^2\}$ of $\{\|a_n - \tilde{a}\|^2\}$ such that $\|a_{n_q} - \tilde{a}\|^2 < \|a_{n_q+1} - \tilde{a}\|^2$ for all $q \in \mathbb{N}$. Define the sequence $\{\tau(n)\}_{n\geq n_0}$ by $\tau(n) := \max\{m \leq n \mid \|a_m - \tilde{a}\|^2 < \|a_{m+1} - \tilde{a}\|^2\}$. According to Lemma 2.5, $\{\tau(n)\}_{n\geq n_0}$ is a nondecreasing sequence with $\lim_{n\to\infty} \tau(n) = \infty$. Additionally, for all $n \geq n_0$, the following estimates hold: $\|a_{\tau(n)} - \tilde{a}\|^2 \leq \|a_{\tau(n)+1} - \tilde{a}\|^2$ and $\|a_n - \tilde{a}\|^2 \leq \|a_{\tau(n)+1} - \tilde{a}\|^2$. Using similar arguments as in **Case 1**, we find that

$$\limsup_{n\to\infty} \langle \phi(\tilde{a}) - \tilde{a}, y_{\tau(n)} - \tilde{a}\rangle \leq 0.$$

From (6) and $\|a_{\tau(n)} - \tilde{a}\|^2 \leq \|a_{\tau(n)+1} - \tilde{a}\|^2$, we obtain

$$\begin{aligned}\|a_{\tau(n)+1} - \tilde{a}\|^2 \leq{}& (1 - \tilde{\alpha}_{\tau(n)})\|a_{\tau(n)+1} - \tilde{a}\|^2 \\ &+ \tilde{\alpha}_{\tau(n)}(1-\varrho)^{-1}[\Xi_{\tau(n)}B_3 + 2\langle \phi(\tilde{a}) - \tilde{a}, y_{\tau(n)} - \tilde{a}\rangle],\end{aligned}$$

which simplifies to

$$\|a_{\tau(n)+1} - \tilde{a}\|^2 \leq (1-\varrho)^{-1}[\Xi_{\tau(n)}B_3 + 2\langle \phi(\tilde{a}) - \tilde{a}, y_{\tau(n)} - \tilde{a}\rangle].$$

Thus, $\limsup_{n\to\infty} \|a_{\tau(n)+1} - \tilde{a}\|^2 \leq 0$, implying $\lim_{n\to\infty} \|a_{\tau(n)+1} - \tilde{a}\|^2 = 0$. Since $\|a_n - \tilde{a}\|^2 \leq \|a_{\tau(n)+1} - \tilde{a}\|^2$, it follows that $\lim_{n\to\infty} \|a_n - \tilde{a}\| = 0$. Therefore, combining results from **Case 1** and **Case 2**, we conclude that $\{a_n\}$ converges strongly to $\tilde{a}$ as $n \to \infty$. □

4. APPLICATION TO DATA CLASSIFICATION PROBLEM

The dataset used in this study was obtained from experimental measurements conducted on clay brick samples with varying physical and compositional properties. Each sample was prepared by systematically altering parameters such as firing temperature, additive content, and particle size distribution. The material

properties—including bulk density, water absorption, and apparent porosity—were measured according to standardized procedures in materials science and engineering. Sound absorption coefficients (SAC) were determined using impedance tube tests across a range of frequencies (250–2000 Hz), in accordance with ISO 10534-2.

For the numerical experiment, the dataset consists of 208 samples and includes seven input attributes: firing temperature, percentage of additive, additive size, bulk density, percentage of water absorption, apparent porosity, and sound frequency. These features were selected as non-acoustic physical properties assumed to influence the prediction of the sound absorption coefficient (α). The SAC values were categorized into five ranges: A (over 0.08), B (0.06–0.079), C (0.04–0.059), D (0.02–0.039), and E (0–0.019), representing varying levels of acoustic performance.

A summary of the attribute definitions and class categories is provided in Table 1.

Table 1: Features of the attributes for sound absorption coefficient prediction

Attribute name	**Description**	**Range**
Firing temperature	Specific temperature at which clay bricks are heated during the firing process (°C)	950 - 1100
Percentage of additive	Percentage of supplementary material incorporated into the clay mixture (%wt)	5 - 30
Additive size	Distribution or range of particle sizes within the additive material (mm.)	0 - 2
Bulk density	Mass of a material relative to its volume, including the spaces between individual particles (g/cm^3)	0.84 - 1.84
Water absorbtion	Material's ability to absorb and retain water when exposed to moisture or submerged in liquid (%)	6.14 - 44.85
Apparent porosity	Proportion of void spaces or pores within a material, expressed as a percentage of the total volume (%)	10.24 - 43.75
Frequency	Number of times per second that a sound pressure wave repeats itself (Hz.)	250 - 2000
SAC (α)	A measure of how much sound energy is absorbed by a material when sound waves strike its surface	A (over 0.08) B (0.06-0.079) C (0.04-0.059) D (0.02-0.039) E (0-0.019)

Extreme Learning Machine (ELM)

We employ the *Extreme Learning Machine (ELM)* method proposed by Huang et al. [**10**], a fast and efficient learning algorithm for single-hidden layer feedforward neural networks (SLFNs). ELM is particularly suitable for regression tasks such as SAC prediction due to its rapid training and strong generalization capabilities.

Given a training dataset

$$S := \{(\mathbf{s}_n, \mathbf{r}_n) : \mathbf{s}_n \in \mathbb{R}^K,\ \mathbf{r}_n \in \mathbb{R}^M,\ n = 1, 2, \ldots, P\},$$

where each $\mathbf{s}_n$ is a non-acoustic input feature vector and $\mathbf{r}_n$ is the corresponding SAC target value, the network approximates the mapping through the following output function of the SLFN with D hidden nodes:

$$\mathbf{Q}_n = \sum_{k=1}^{D} E_k \, V(c_k \mathbf{s}_n + d_k),$$

where V is the activation function, c_k and d_k are the input weight matrix and bias vector of the k-th hidden node, respectively, and E_k denotes the output weight to be optimized.

To solve for the optimal output weights, the hidden layer output matrix L is constructed as:

$$L = \begin{bmatrix} V(c_1\mathbf{s}_1 + d_1) & \cdots & V(c_D\mathbf{s}_1 + d_D) \\ \vdots & \ddots & \vdots \\ V(c_1\mathbf{s}_P + d_1) & \cdots & V(c_D\mathbf{s}_P + d_D) \end{bmatrix}.$$

In our application, ELM plays a key role in predicting the sound absorption coefficient (SAC) of materials by learning a nonlinear mapping from easily measurable physical properties to SAC values. This approach provides a practical and computationally efficient alternative to conventional experimental methods.

To solve ELM is to find optimal output weight $E = [E_1^T, ..., E_D^T]^T$ such that $LE = T$, where $T = [\mathbf{r}_1^T, ..., \mathbf{r}_P^T]^T$ is the training data. In some cases, finding $E = L^\dagger T$, where $L^\dagger$ is the *Moore-Penrose generalized inverse* of L. We can solve $LE = T$ by the following the least squares problem

$$\min_{E \in \mathbb{R}^D} \{\frac{1}{2}\|LE - T\|_2^2 + \lambda \|E\|_1\}, \tag{12}$$

when λ is a regularization parameter. This problem is well recognized as the least absolute shrinkage and selection operator (LASSO) [**27**].

By applying the least squares regularization, we construct four models as follows:

1. The least squares model — ($M1$)

$$\min_{E \in \mathbb{R}^D} \frac{1}{2}\|LE - T\|_2^2. \tag{13}$$

To utilize our proposed algorithm, we define

$$XE = \nabla \left(\frac{1}{2}\|LE - T\|_2^2 \right) = L^\top (LE - T), \quad Y = 0.$$

2. The regularized least squares model — ($M2$)

$$\min_{E \in \mathbb{R}^D} \left\{ \frac{1}{2}\|LE - T\|_2^2 + \lambda \|E\|_1 \right\}, \tag{14}$$

where $\lambda > 0$.
We define

$$XE = L^{\top}(LE - T), \quad Y = \lambda \cdot \partial \|E\|_1,$$

where $\partial \|E\|_1$ denotes the subgradient of the ℓ_1 norm.

3. The least squares model on constraint set L_2 — ($M3$)

$$\min_{E \in S} \frac{1}{2} \|LE - T\|_2^2, \tag{15}$$

where $S = \{E \in \mathbb{R}^D : \|E\|_2^2 \leq r\}$.
To adapt this model to our algorithm, we set

$$XE = L^{\top}(LE - T).$$

4. The regularized least squares model on constraint set L_2 — ($M4$)

$$\min_{E \in S} \left\{ \frac{1}{2} \|LE - T\|_2^2 + \lambda \|E\|_1 \right\}, \tag{16}$$

where $S = \{E \in \mathbb{R}^D : \|E\|_2^2 \leq r\}$ and $\lambda > 0$.
We define

$$XE = L^{\top}(LE - T), \quad YE = \lambda \cdot \partial \|E\|_1.$$

In this research, we utilize the multi-class cross-entropy loss function ($H(y, p)$), where W is the number of classes, y_k is the true label for class k, p_k is the predicted probability for class k, and the formula as follows:

$$H(y, p) = -\sum_{k=1}^{W} y_k \cdot \log(p_k).$$

To consider the performance of algorithm, we have four measures to estimate [**26**] are denoted as follows:

$$\text{Precision(Pre)} = \frac{TP}{TP + FP} \times 100\%. \tag{17}$$

$$\text{Recall(Rec)} = \frac{TP}{TP + FN} \times 100\%. \tag{18}$$

$$\text{Accuracy(Acc)} = \frac{TP + TN}{TP + FP + TN + FN} \times 100\%, \tag{19}$$

where TP is True Positive, TN is True Negative, FP is False Positives, and FN is False Negatives. Likewise, N and P are the Negative, and Positive population of Malignant and Benign cases, respectively. We defines F-Measure is the harmonic mean value between recall and precision as follows:

$$\text{F1-Score} = 2 \left(\frac{\text{Precision} \times \text{Recall}}{\text{Precision} + \text{Recall}} \right) \times 100\%. \tag{20}$$

We set the activation function as sigmoid, hidden nodes $D = 180$, $\lambda = 10^{-7}$ and N is the iteration number. For Algorithm 1, 2, and 3,

$$\alpha_n = \begin{cases} \overline{\alpha_n}, & \text{if } n > N, \\ 0.5, & \text{otherwise} \end{cases}$$

where $\overline{\alpha_n} = \frac{n}{2n^2+1}$.
For Algorithm 1,

$$\theta_n = \begin{cases} \frac{1}{n^3}, & \text{if } n > N, \\ \overline{\theta}, & \text{otherwise.} \end{cases}$$

where $\overline{\theta} = 0.8$ and $\mu_1 = \frac{0.9999}{max(eigenvalue(A^T A)}$.
For Algorithm 2, and 3,

$$\theta_n = \begin{cases} \frac{1}{\|a_n - a_{n-1}\| n^3}, & \text{if } a_n \neq a_{n-1} \text{ and } n > N, \\ \overline{\theta}, & \text{otherwise,} \end{cases}$$

and

$$\delta_n = \begin{cases} \frac{1}{\|a_{n-1} - a_{n-2}\| n^3}, & \text{if } a_{n-1} \neq a_{n-2} \text{ and } n > N, \\ \overline{\delta}, & \text{otherwise,} \end{cases}$$

where $\overline{\theta} = 0.8$, $\overline{\delta} = 0.5$, and $\mu_n = \frac{0.9999}{max(eigenvalue(A^T A)}$.

We split the datasets into five test boxes. We have 80% of training datasets and 20% of testing datasets. In Table 1 - 5, we compare our algorithm with the literature method. For the different r, Test box 1: $r = 3$, Test box 2: $r = 50$, Test box 3: $r = 410$, Test box 4: $r = \sqrt{2}$, and Test box 5: $r = 270$.

Table 1: The numerical results of the datasets of each algorithm in Test box 1

Test box 1	**Iter**	**Acc** (%)	**Pre** (%)	**Rec** (%)	**F1** (%)	**Time**
Algorithm 1 M1	290	77.14	87.50	85.70	86.59	0.5591
Algorithm 1 M2	290	77.14	87.50	85.70	86.59	0.5605
Algorithm 1 M3	290	77.14	87.50	85.70	86.59	0.5625
Algorithm 1 M4	290	77.14	87.50	85.70	86.59	0.5651
Algorithm 2 M1	290	71.43	NaN	80.00	NaN	0.0830
Algorithm 2 M2	290	71.43	NaN	80.00	NaN	0.0842
Algorithm 2 M3	290	71.43	NaN	80.00	NaN	0.0868
Algorithm 2 M4	290	71.43	NaN	80.00	NaN	0.0869
Algorithm 3 M1	47	86.67	92.20	91.45	91.82	0.0231
Algorithm 3 M2	47	86.67	92.20	91.45	91.82	0.0360
Algorithm 3 M3	31	86.67	92.20	91.45	91.82	0.0198
Algorithm 3 M4	31	86.67	92.20	91.45	91.82	0.0136

Table 1 shows that Algorithm 3 M4 is the best overall. It achieves the highest accuracy (86.67%), precision (92.20%), recall (91.45%), and F1-score (91.82%) while having the fastest computation time with 31^{th} iteration.

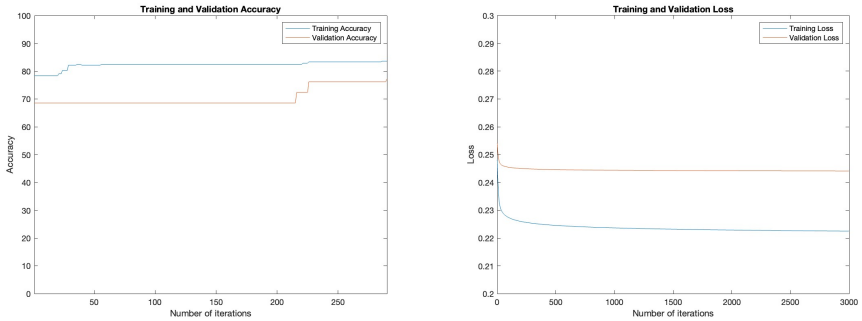

Figure 1: On the left is the training and validation accuracy of Algorithm 1 and on the right is the training and validation loss of Algorithm 1.

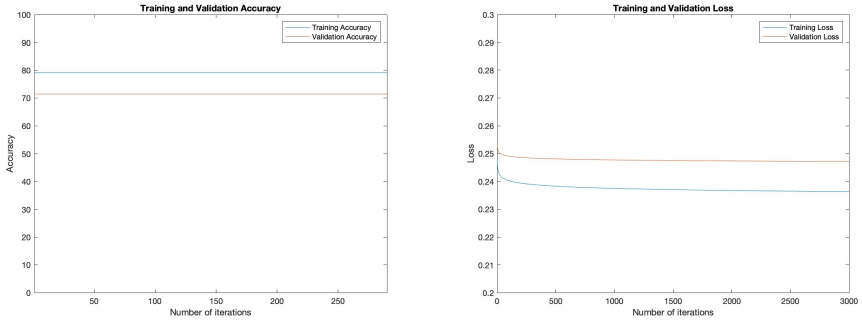

Figure 2: On the left is the training and validation accuracy of Algorithm 2 and on the right is the training and validation loss of Algorithm 2.

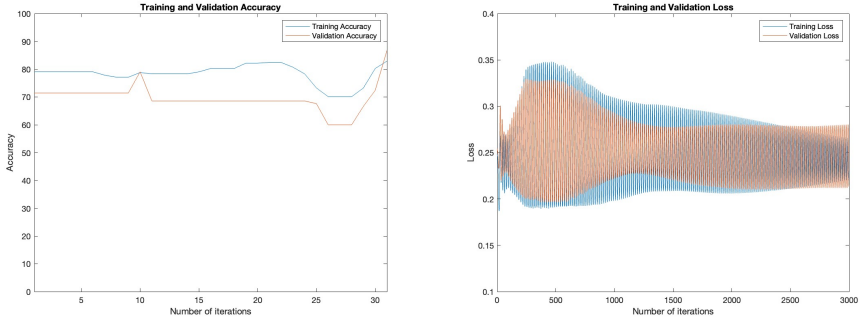

Figure 3: On the left is the training and validation accuracy of Algorithm 3 and on the right is the training and validation loss of Algorithm 3.

Figures 1-3 highlight training and validation results for three algorithms. Algorithm 1 and Algorithm 2 show stable but lower accuracy. Algorithm 3 outperforms both with higher accuracy, better alignment between training and validation, and effective loss reduction despite some fluctuations.

Table 2: The numerical results of the datasets of each algorithm in Test box 2

Test box 2	**Iter**	**Acc** (%)	**Pre** (%)	**Rec** (%)	**F1** (%)	**Time**
Algorithm 1 M1	237	78.10	86.24	85.38	85.81	0.4577
Algorithm 1 M2	237	78.10	86.24	85.38	85.81	0.4583
Algorithm 1 M3	237	78.10	86.24	85.38	85.81	0.4662
Algorithm 1 M4	237	78.10	86.24	85.38	85.81	0.4620
Algorithm 2 M1	237	72.38	85.95	80.69	83.24	0.0699
Algorithm 2 M2	237	72.38	85.95	80.69	83.24	0.0700
Algorithm 2 M3	237	72.38	85.95	80.69	83.24	0.0714
Algorithm 2 M4	237	72.38	85.95	80.69	83.24	0.0728
Algorithm 3 M1	43	86.67	92.55	91.40	91.97	0.0235
Algorithm 3 M2	43	86.67	92.55	91.40	91.97	0.0272
Algorithm 3 M3	31	89.52	94.01	93.13	93.57	0.0178
Algorithm 3 M4	31	89.52	94.01	93.13	93.57	0.0146

Table 2 shows that Algorithm 3 M4 is the best overall. It achieves the highest accuracy (89.52%), precision (94.01%), recall (93.13%), and F1-score (93.57%) while having the fastest computation time with 31^{th} iteration.

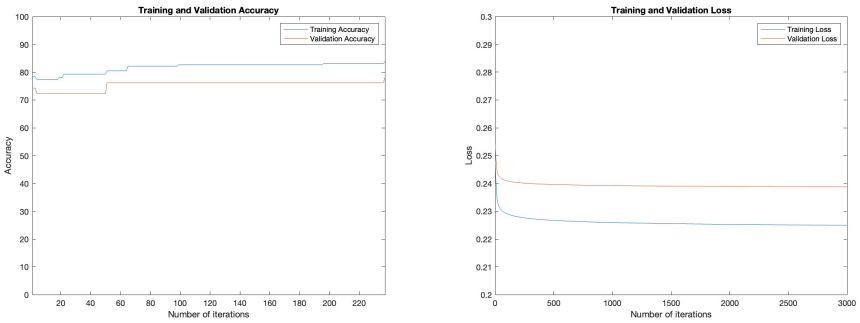

Figure 4: On the left is the training and validation accuracy of Algorithm 1 and on the right is the training and validation loss of Algorithm 1.

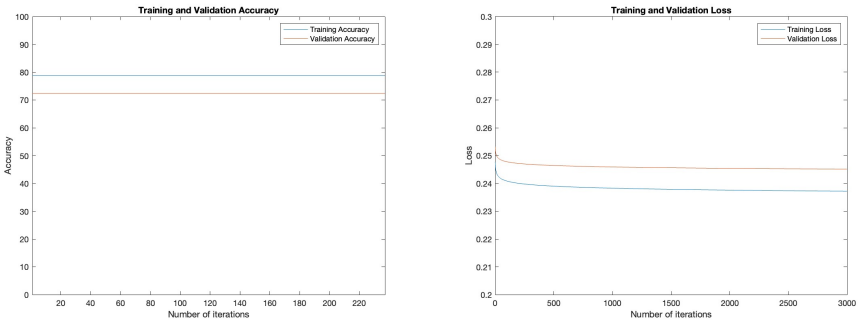

Figure 5: On the left is the training and validation accuracy of Algorithm 2 and on the right is the training and validation loss of Algorithm 2.

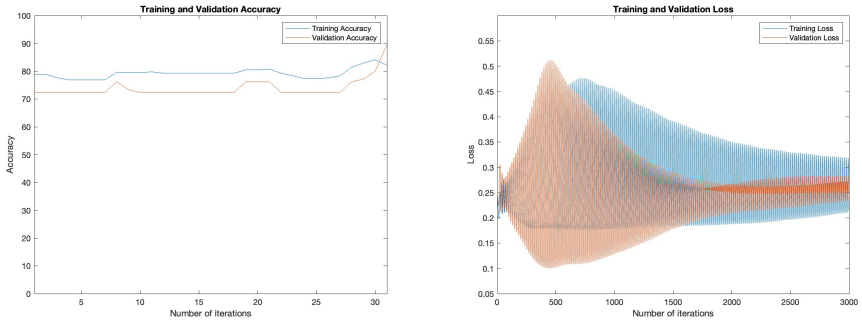

Figure 6: On the left is the training and validation accuracy of Algorithm 3 and on the right is the training and validation loss of Algorithm 3.

Figures 4-6 represent Algorithm 1, and Algorithm 2 displays steady improvements in accuracy but lags behind Algorithm 3 in terms of overall performance. Algorithm 3 achieves superior accuracy and demonstrates better alignment between training and validation data, indicating stronger generalization. The loss reduction for Algorithm 3 is more pronounced, suggesting higher efficiency and convergence speed.

Table 3: The numerical results of the datasets of each algorithm in Test box 3

Test box 3	**Iter**	**Acc** (%)	**Pre** (%)	**Rec** (%)	**F1** (%)	**Time**
Algorithm 1 M1	33	90.48	94.50	93.64	94.07	0.0677
Algorithm 1 M2	33	90.48	94.50	93.64	94.07	0.0685
Algorithm 1 M3	33	90.48	94.50	93.64	94.07	0.0678
Algorithm 1 M4	33	90.48	94.50	93.64	94.07	0.0681
Algorithm 2 M1	33	81.90	90.95	87.42	89.15	0.0996
Algorithm 2 M2	33	81.90	90.95	87.42	89.15	0.0167
Algorithm 2 M3	33	81.90	90.95	87.42	89.15	0.0170
Algorithm 2 M4	33	81.90	90.95	87.42	89.15	0.0128
Algorithm 3 M1	15	91.43	95.19	94.20	94.69	0.0086
Algorithm 3 M2	15	91.43	95.19	94.20	94.69	0.0095
Algorithm 3 M3	15	91.43	95.19	94.20	94.69	0.0066
Algorithm 3 M4	15	91.43	95.19	94.20	94.69	0.0081

Table 3 shows that Algorithm 3 M3 is the best overall. It achieves the highest accuracy (91.43%), precision (95.19%), recall (94.20%), and F1-score (94.69%) while having the fastest computation time with 15^{th} iteration.

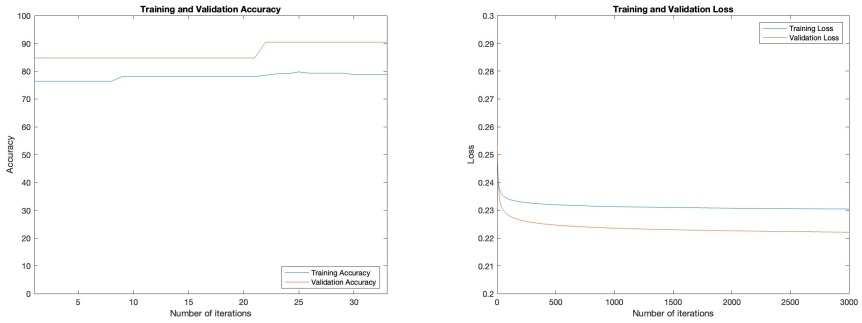

Figure 7: On the left is the training and validation accuracy of Algorithm 1 and on the right is the training and validation loss of Algorithm 1.

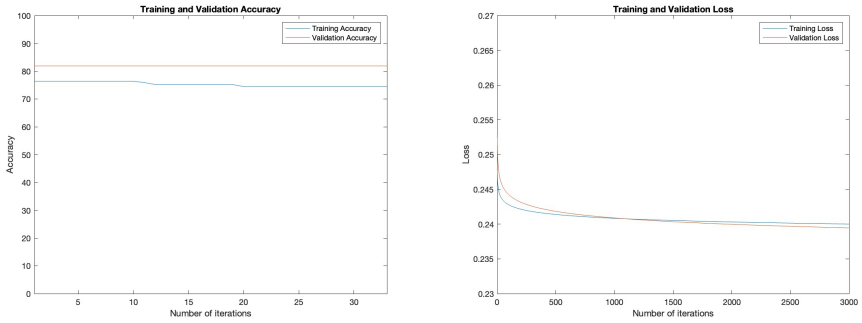

Figure 8: On the left is the training and validation accuracy of Algorithm 2 and on the right is the training and validation loss of Algorithm 2.

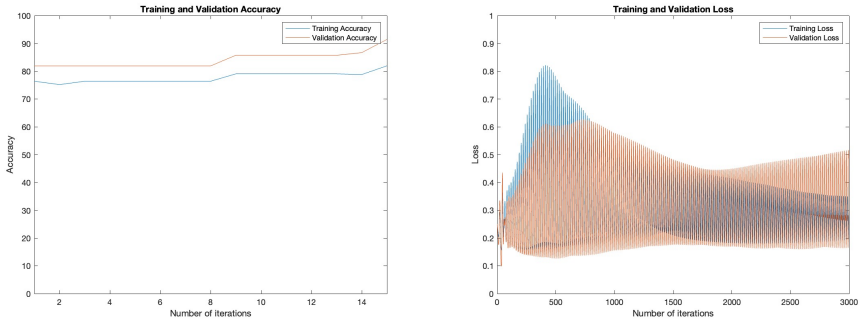

Figure 9: On the left is the training and validation accuracy of Algorithm 3 and on the right is the training and validation loss of Algorithm 3.

The training and validation accuracy and loss trends for Figures 7-9 further emphasize the advantages of Algorithm 3 over the other two. While Algorithm 1 and Algorithm 2 show slower convergence and some instability in validation performance, Algorithm 3 maintains consistent accuracy improvements with minimal fluctuations. This stability highlights Algorithm 3's robustness across varying datasets, particularly in complex classification tasks.

Table 4: The numerical results of the datasets of each algorithm in Test box 4

Test box 4	**Iter**	**Acc** (%)	**Pre** (%)	**Rec** (%)	**F1** (%)	**Time**
Algorithm 1 M1	18	74.63	85.13	82.74	83.92	0.0403
Algorithm 1 M2	18	74.63	85.13	82.74	83.92	0.0391
Algorithm 1 M3	255	74.63	85.56	84.59	85.07	0.5025
Algorithm 1 M4	255	74.63	85.56	84.59	85.07	0.5031
Algorithm 2 M1	18	74.63	85.13	82.74	83.92	0.0129
Algorithm 2 M2	18	74.63	85.13	82.74	83.92	0.0095
Algorithm 2 M3	255	74.63	85.13	82.74	83.92	0.0784
Algorithm 2 M4	255	74.63	85.13	82.74	83.92	0.0786
Algorithm 3 M1	18	74.63	86.03	83.76	84.88	0.1057
Algorithm 3 M2	18	74.63	86.03	83.76	84.88	0.0105
Algorithm 3 M3	255	87.32	92.64	91.73	92.18	0.0776
Algorithm 3 M4	255	87.32	92.64	91.73	92.18	0.0785

Table 4 shows that Algorithm 3 M3 is the best overall. It achieves the highest accuracy (87.32%), precision (92.64%), recall (91.73%), and F1-score (92.18%) with 255^{th} iteration.

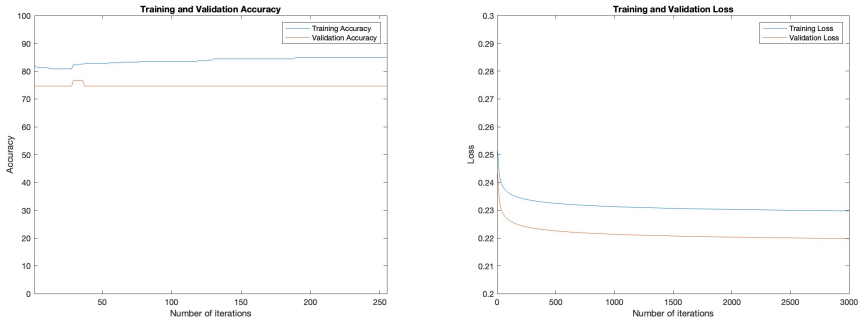

Figure 10: On the left is the training and validation accuracy of Algorithm 1 and on the right is the training and validation loss of Algorithm 1.

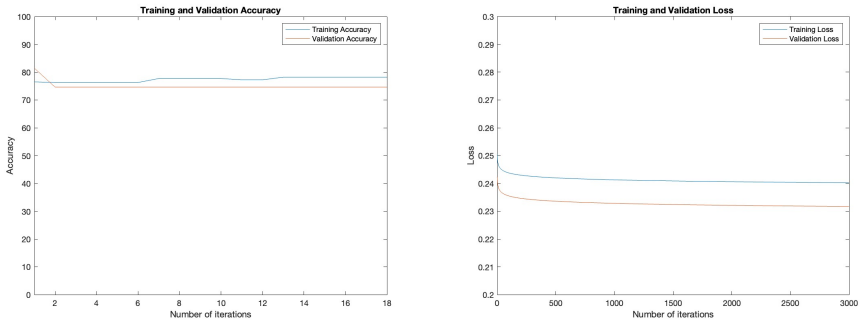

Figure 11: On the left is the training and validation accuracy of Algorithm 2 and on the right is the training and validation loss of Algorithm 2.

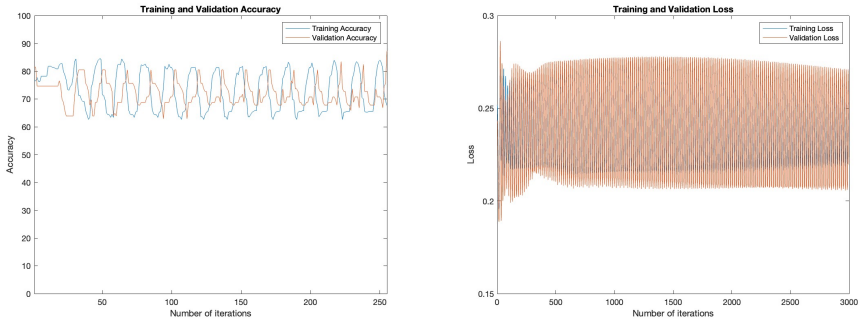

Figure 12: On the left is the training and validation accuracy of Algorithm 3 and on the right is the training and validation loss of Algorithm 3.

Figures 10-12, Algorithm 1 continues to underperform, struggling with higher validation loss, while Algorithm 2 slightly improves. Algorithm 3 consistently achieves the highest training and validation accuracy and shows a steady decline in loss, reinforcing its suitability for more demanding tasks.

Table 5: The numerical results of the datasets of each algorithm in Test box 5

Test box 5	**Iter**	**Acc** (%)	**Pre** (%)	**Rec** (%)	**F1** (%)	**Time**
Algorithm 1 M1	104	70.73	84.98	80.60	82.73	0.2059
Algorithm 1 M2	104	70.73	84.98	80.60	82.73	0.2084
Algorithm 1 M3	104	70.73	84.98	80.60	82.73	0.2078
Algorithm 1 M4	104	70.73	84.98	80.60	82.73	0.2045
Algorithm 2 M1	104	69.76	NaN	80.00	NaN	0.0374
Algorithm 2 M2	104	69.76	NaN	80.00	NaN	0.0412
Algorithm 2 M3	104	69.76	NaN	80.00	NaN	0.0335
Algorithm 2 M4	104	69.76	NaN	80.00	NaN	0.0804
Algorithm 3 M1	46	73.66	84.38	83.13	83.75	0.0210
Algorithm 3 M2	46	73.66	84.38	83.13	83.75	0.0155
Algorithm 3 M3	75	80.49	90.24	86.92	88.55	0.0286
Algorithm 3 M4	75	80.49	90.24	86.92	88.55	0.0291

Table 5 shows that Algorithm 3 M3 is the best overall. It achieves the highest accuracy (80.49%), precision (90.24%), recall (86.92%), and F1-score (88.55%) with 75^{th} iteration.

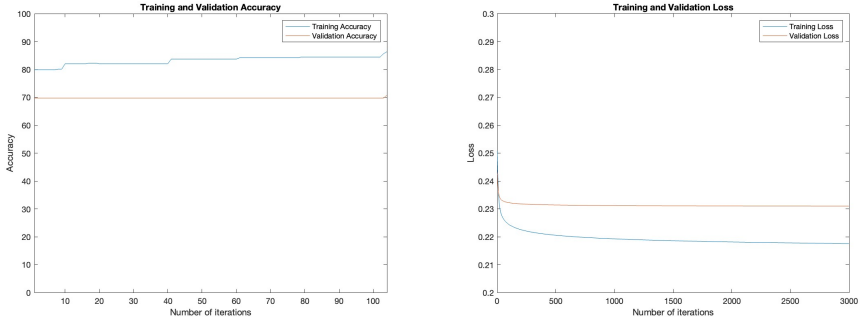

Figure 13: On the left is the training and validation accuracy of Algorithm 1 and on the right is the training and validation loss of Algorithm 1.

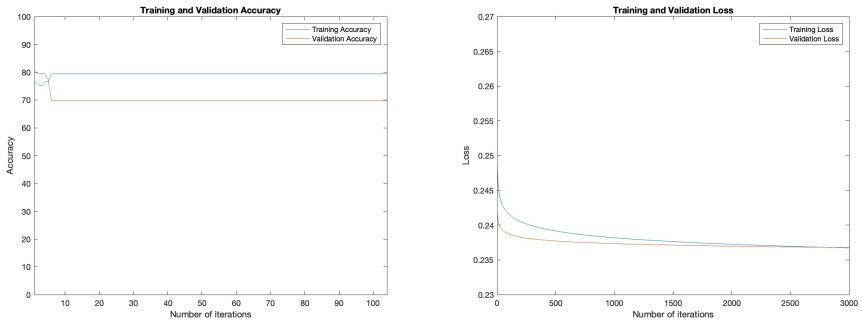

Figure 14: On the left is the training and validation accuracy of Algorithm 2 and on the right is the training and validation loss of Algorithm 2.

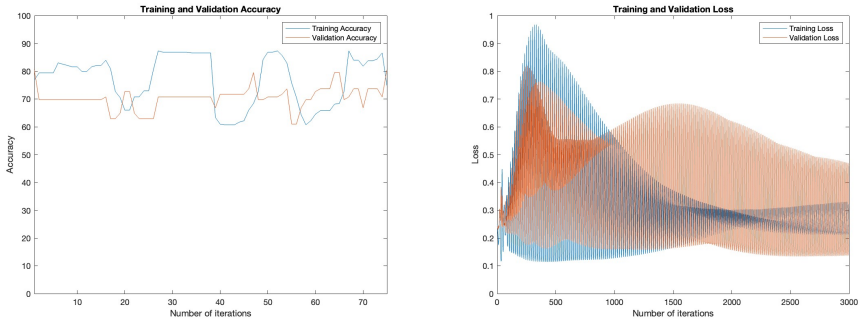

Figure 15: On the left is the training and validation accuracy of Algorithm 3 and on the right is the training and validation loss of Algorithm 3.

Figures 13-15 show that Algorithm 3's accuracy trends stay significantly above those of Algorithm 1 and Algorithm 2. The validation loss for Algorithm 3 drops uniformly, indicating minimal overfitting. On the contrary, Algorithm 1 and Algorithm 2 display less uniformity in performance, with noticeable gaps between training and validation metrics.

Remark 4.7. The fluctuations in validation loss and accuracy for Algorithm 3 (Figures 3, 6, 9, 12, and 15) stem from its dynamic structure, which incorporates inertial and adaptive components. This design—proposed by the authors—enhances convergence speed and overall performance, as supported by the highest accuracy and F1 score in Table 1.

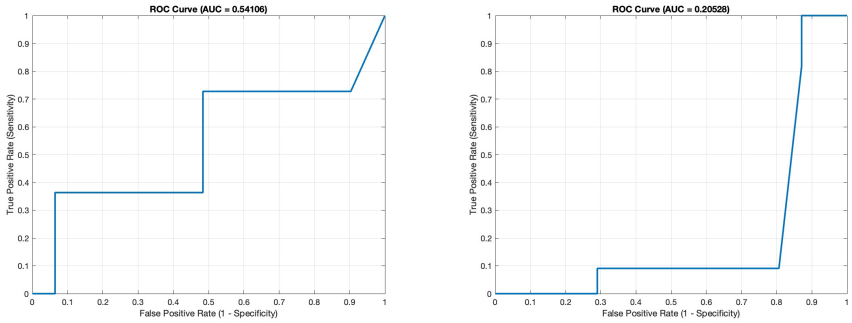

Figure 16: On the left is the ROC curve of Algorithm 3 in Test box 1 and on the right is the ROC curve of Algorithm 3 in Test box 2

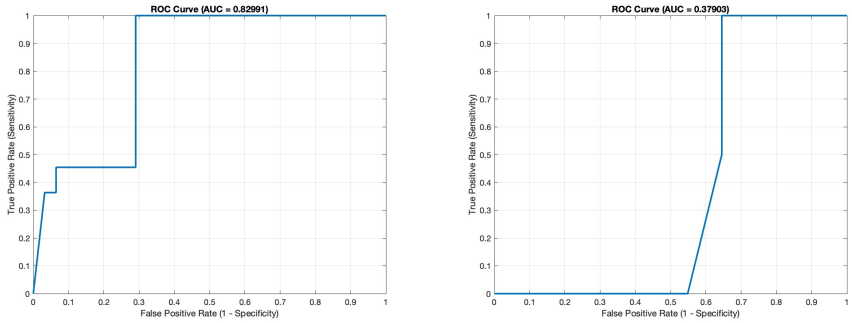

Figure 17: On the left is the ROC curve of Algorithm 3 in Test box 3 and on the right is the ROC curve of Algorithm 3 in Test box 4

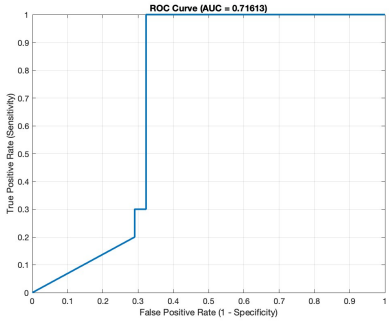

Figure 18: The ROC curve of Algorithm 3 in Test box 5

From Figures 16-18, Test box 3 is the best for Algorithm 3, as its ROC curve shows the highest AUC, indicating superior classification performance. The ROC curve is crucial as it visualizes the trade-off between sensitivity and specificity across different thresholds, helping evaluate and optimize model performance. Test box 3 achieves the best balance, minimizes false positives, and ensures stable and reliable predictions, making it the most suitable choice for data classification tasks.

5. CONCLUSION

This study investigated a novel approach for predicting the sound absorption coefficient (SAC; α) of materials using non-acoustic parameters, alongside the development and application of advanced mathematical algorithms. Traditional methods for SAC measurement, such as the reverberation room method and impedance tube method, require specialized equipment and controlled environments, making them time-intensive and costly. By leveraging easily measurable physical properties such as density, water absorption, porosity, and additive characteristics, we developed a predictive framework that offers a cost-effective alternative.

To enhance prediction accuracy, we implemented various mathematical models and machine learning algorithms, comparing their performance based on accuracy, precision, recall, and F1-score. The results demonstrated that Algorithm 3 M4 consistently achieved superior performance, offering the highest classification accuracy while maintaining minimal computational complexity. These findings reinforce the feasibility of using non-acoustic parameters for SAC estimation, paving the way for more accessible acoustic material evaluation techniques.

From a mathematical perspective, this study contributed to the variational inclusion problem (VIP) by applying and analyzing forward-backward and Tseng's splitting methods. Our proposed algorithms were designed to improve computational efficiency, convergence rates, and numerical stability in solving complex inclusion problems. Our numerical experiments validated the effectiveness of these approaches, particularly highlighting the robust performance of the Two Inertial Projective Mann Forward-Backward Algorithm (TIPMFB) and the Inertial Modified Relaxed Forward-Backward (IMRFB) method.

Overall, the integration of mathematical optimization techniques with data-driven SAC prediction models demonstrates a promising interdisciplinary approach. Future research could extend these findings by incorporating deep learning models, expanding the dataset with a broader range of material compositions, and refining the variational inclusion framework for further optimization in both mathematical and engineering applications.

Acknowledgments N. Jun-on and S. Lawanwadeekul would like to thank Thailand Science Research and Innovation, 2026 Fundamental Fund, Lampang Rajabhat University (Grant No. 033/2569). W. Yajai and W. Cholamjiak would like to thank University of Phayao and Thailand Science Research and Innovation Fund (Fundamental Fund 2026, Grant No. 2253/2568).

REFERENCES

1. J. F. Allard, Y. Champoux: *New empirical equations for sound propagation in rigid frame fibrous materials.* J. Acoust. Soc. Am., **91(6)** (1992), 3346–3353.
2. H. H. Bauschke, P. L. Combettes: *Convex analysis and monotone operator theory in Hilbert spaces.* CMS Books in Mathematics, Springer, 2017.
3. H. Brézis: *Opérateurs maximaux monotones et semi-groupes de contractions dans les espaces de Hilbert.* Mathematical Studies (Vol. 5), North-Holland, 1973.

4. P. Cholamjiak, D. V. Hieu, Y. J. Cho: *Relaxed forward-backward splitting methods for solving variational inclusions and applications.* J. Sci. Comput., **88(3)** (2021), Article 85.

5. W. Cholamjiak, P. Cholamjiak, S. Suantai: *An inertial forward-backward splitting method for solving inclusion problems in Hilbert spaces.* J. Fixed Point Theory Appl., **20(1)** (2018), 42.

6. P. L. Combettes, V. R. Wajs: *Signal recovery by proximal forward-backward splitting.* Multiscale model. simul., **4(4)** (2005), 1168–1200.

7. T. Cox, P. d'Antonio: *Acoustic absorbers and diffusers: Theory, design and application.* CRC Press, 2016.

8. C. Garodia, I. Uddin, D. Baleanu: *On constrained minimization, variational inequality and split feasibility problem via new iteration scheme in Banach spaces.* Bull. Iran. Math. Soc., **48(4)** (2022), 1493–1512.

9. A. Gibali, D. V. Thong: *Tseng type methods for solving inclusion problems and its applications.* Calcolo, **55** (2018), 1–22.

10. G. B. Huang, Q. Y. Zhu, C. K. Siew: *Extreme learning machine: Theory and applications.* Neurocomputing, **70(1–3)** (2006), 489–501.

11. O. S. Iyiola, Y. Shehu: *Convergence results of two-step inertial proximal point algorithm.* Appl. Numer. Math., **182** (2022), 57–75.

12. S. Kesornprom, P. Cholamjiak: *A new relaxed inertial forward-backward-forward method for solving the convex minimization problem with applications to image inpainting.* Appl. Set-Valued Anal. Optim., **5** (2023), 439–450.

13. S. Lawanwadeekul, T. Otsuru, R. Tomiku, H. Nishiguchi, N. Sakamoto, D. Matsuoka, R. Yoshimoto: *Applying the ensemble averaging method with a pressure–velocity sensor to measure sound absorption characteristics of porous clay bricks.* Appl. Acoust., **164** (2020), 107250.

14. S. Lawanwadeekul, P. Torkittikul, S. Mulinta, T. Khunyotying, W. Tasang, M. Bunma: *Effect of size and amount of lightweight expanded clay aggregate on normal incidence sound absorption coefficient of concrete.* Eng. Appl. Sci. Res., **50(3)** (2023), 195–201.

15. P. L. Lions, B. Mercier: *Splitting algorithms for the sum of two nonlinear operators.* SIAM J. Numer. Anal., **16(6)** (1979), 964–979.

16. D. A. Lorenz, T. Pock: *An inertial forward-backward algorithm for monotone inclusions.* J. Math. Imaging Vis., **51(2)** (2015), 311–325.

17. P. E. Maingé: *Strong convergence of projected subgradient methods for nonsmooth and nonstrictly convex minimization.* Set-Valued Anal., **16** (2008), 899–912.

18. A. Moudafi: *Viscosity approximation methods for fixed-points problems.* J. Math. Anal. Appl., **241(1)** (2000), 46–55.

19. N. Petrot, M. Khonchaliew, M. Suwannaprapa: *Modified inertial Tseng type method for zeros of the sum of monotone operators in Hilbert spaces.* Carpathian J. Math., **40(2)** (2024), 399–417.

20. A. Padcharoen, D. Kitkuan, W. Kumam, P. Kumam: *Tseng methods with inertia for solving inclusion problems and application to image deblurring and image recovery problems.* Comput. Math. Methods, **3(3)** (2021).

21. G. B. Passty: *Ergodic convergence to a zero of the sum of monotone operators in Hilbert space.* J. Math. Anal. Appl., **72(2)** (1979), 383–390.

22. P. Peeyada, P. Kitisak, W. Cholamjiak, D. Yambangwai: *Two inertial projective Mann forward-backward algorithms for variational inclusion problems and application to stroke prediction.* Carpathian J. Math., **40(2)** (2024).

23. P. Peeyada, R. Suparatulatorn, W. Cholamjiak: *An inertial Mann forward-backward splitting algorithm of variational inclusion problems and its applications.* Chaos, Solitons & Fractals, **158** (2022), 112048.

24. R. Suparatulatorn, A. Khemphet: *Tseng-type methods for inclusion and fixed point problems with applications.* Mathematics, **7(12)** (2019), 1175.

25. W. Takahashi: *Nonlinear functional analysis.* Yokohama Publishers, Yokohama, 2000.

26. T. Thomas, N. Pradhan, V. S. Dhaka: *Comparative analysis to predict breast cancer using machine learning algorithms: A survey.* In: 2020 International Conference on Inventive Computation Technologies (ICICT), IEEE, (2020), 192–196.

27. R. Tibshirani: *Regression shrinkage and selection via the lasso.* J. R. Stat. Soc. Ser. B Stat. Methodol., **58** (1996), 267–288.

28. P. Tseng: *A modified forward-backward splitting method for maximal monotone mappings.* SIAM J. Control Optim., **38(2)** (2000), 431–446.

29. H. K. Xu: *Iterative algorithms for nonlinear operators.* J. Lond. Math. Soc., **66** (2002), 240–256.

30. S. S. Zhang, J. H. Lee, C. K. Chan: *Algorithms of common solutions to quasi variational inclusion and fixed point problems.* Appl. Math. Mech., **29(5)** (2008), 571–581.

31. International Organization for Standardization: *ISO 354:2024 Acoustics — Measurement of sound absorption in a reverberation room.* ISO, 2024.

32. International Organization for Standardization: *ISO 10534-2:1998, Acoustics—Determination of sound absorption coefficient and impedance in impedance tubes—Part 2: Transfer function method.* ISO, 1998.

Raweerote Suparatulatorn
Department of Mathematics,
Faculty of Science,
Lampang Rajabhat University,
Lampang 52100, Thailand
E-mail: *raweerote.s@gmail.com*
https://orcid.org/0000-0003-0790-3811

(Received 14.02.2025.)
(Revised 05.12.2025.)

Nipa Jun-on
Department of Mathematics,
Faculty of Science,
Lampang Rajabhat University,
Lampang 52100, Thailand
E-mail: *nipa.676@g.lpru.ac.th*
https://orcid.org/0000-0002-2908-7715

Siwat Lawanwadeekul
Faculty of Industrial Technology,
Lampang Rajabhat University,
Lampang 52100, Thailand
E-mail: *b_siwat@g.lpru.ac.th*
https://orcid.org/0000-0002-0827-0078

Watcharaporn Yajai
School of Science,
University of Phayao,
Phayao 56000, Thailand
E-mail: *watcharaporn.yajai@gmail.com*
https://orcid.org/0000-0001-7670-7940

Watcharaporn Cholamjiak
School of Science,
University of Phayao,
Phayao 56000, Thailand
E-mail: *watcharaporn.ch@up.ac.th*
https://orcid.org/0000-0002-8563-017X